SUPPLEMENTARY INFORMATION

Soderberg *et al.*, Nature Manuscript 2008-02-01442

1 Spectral analysis of *Swift*/XRT data

We use the `xspec` v11.3.2 X-ray spectral fitting package to fit both a power law and a blackbody model to the XRT outburst data. In both models we allow for excess neutral hydrogen absorption (N_H) above the Galactic value along the line of sight to NGC 2770, $N_{H,\rm Gal} = 1.7 \times 10^{20}$ cm^{-2}. The best-fit power law model ($\chi^2 = 7.5$ for 17 degrees of freedom; probability, $P = 0.98$) has a photon index, $\Gamma = 2.3 \pm 0.3$ (or, $F_\nu \propto \nu^{-1.3\pm0.3}$) and $N_H = 6.9^{+1.8}_{-1.5} \times 10^{21}$ cm^{-2}. The best-fit blackbody model is described by $kT = 0.71 \pm 0.08$ keV and $N_H = 1.3^{+1.0}_{-0.9} \times 10^{21}$ cm^{-2}. However, this model provides a much poorer fit to the data ($\chi^2 = 26.0$ for 17 degrees of freedom; probability, $P = 0.074$). We therefore adopt the power law model as the best description of the data. The resulting count rate to flux conversion is 1 counts s^{-1} $= 5 \times 10^{-11}$ erg cm^{-2} s^{-1}. The outburst undergoes a significant hard-to-soft spectral evolution as indicated by the ratio of counts in the $0.3-2$ keV band and $2-10$ keV band. The hardness ratio decreases from 1.35 ± 0.15 during the peak of the flare to 0.25 ± 0.10 about 400 s later. In the context of the power law model this spectral softening corresponds to a change from $\Gamma = 1.70 \pm 0.25$ to 3.20 ± 0.35 during the same time interval.

2 High resolution optical spectroscopy

We obtained the spectrum with the High Resolution Echelle Spectrometer (HIRES) mounted on the Keck I 10-m telescope beginning at Jan 17.46 UT. A total of four 1800-s exposures were obtained with a spectral resolution, $R = 48,000$, and a slit width of 0.86 arcsec. The data reach a signal-to-noise ratio of 18 per pixel. We reduced the data with the MAKEE reduction package. We are interested in the Na I D and K I absorption features since they are sensitive to the gas column density, and hence extinction, along the line of the sight to the SN.

The continuum-normalized spectra are plotted against the velocity relative to the rest-frame of NGC 2770 (Figure 2). The positive velocity for the Na I and K I features indicates

a rotation velocity at the position of the SN of 150 km s^{-1}. While the Na I lines are saturated, the weaker K I lines reveal two distinct unsaturated components with equivalent widths of $\mathrm{EW}_1 = 0.08$ Å and $\mathrm{EW}_2 = 0.09$ Å. This indicates[45] a best value for the differential extinction of $E(B-V) \approx 0.7$ mag, with a plausible range that accounts for the scatter in the relation of $0.4 < E(B-V) < 0.8$ mag. With the standard Milky Way extinction curve this corresponds[46] to a V-band extinction of $1.4 < A_V < 2.8$ mag. This range is consistent with the estimate of the extinction based on the hydrogen column density inferred from the X-ray analysis.

3 Rejecting a Relativistic Origin for XRO 080109

We investigate the possibility that XRO 080109 is the result of a relativistic outflow similar to that in GRBs. In this context the emission is non-thermal synchrotron radiation. The outburst flux density is 7.5×10^2 μJy at 0.3 keV. Simultaneously, we find 3σ limits on the flux density in the UBV bands (~ 3 eV) of $F_\nu < 9.0 \times 10^2$ μJy, indicating that the peak of the synchrotron spectrum must be located between the UV and X-ray bands. In the standard synchrotron model this requires the frequencies corresponding to electrons with the minimum and cooling Lorentz factors to obey $\nu_m \approx \nu_c \approx 3 \times 10^{16}$ Hz, while the peak of the spectrum is $F_{\nu,\mathrm{p}} \approx 3$ mJy.

The inferred values of ν_m and ν_c allow us to constrain[47] the outflow parameters and thus to check for consistency with the hypothesis of relativistic expansion. The relevant parameters are the bulk Lorentz factor (γ), the magnetic field (B), and the shock radius (R_{sh}). From the value of ν_c we find $\gamma B^3 \approx 8.3 \times 10^3$, and since $\gamma > 1$ we conclude that $B < 20$ G. In addition, using ν_m we find $\epsilon_e^2 \gamma^3 B \approx 3 \times 10^4$; here ϵ_e is the fraction of post-shock energy in the relativistic electrons. Along with the constraint on B, we infer $\gamma > 25$. Indeed, for a typical $\epsilon_e = 0.1$ the values are $B \approx 4.5$ G and $\gamma \approx 90$. Finally, the peak flux is given by $F_{\nu,\mathrm{p}} \approx 5.4 \gamma B A_* (R_{\mathrm{sh}}/10^{10}\,\mathrm{cm})$ μJy, where A_* is the wind density parameter and a value of unity corresponds to a mass loss rate, $\dot{M} = 10^{-5}$ M$_\odot$ yr^{-1}, with a velocity of $v_w = 10^3$ km s^{-1}. Comparing to the measured flux we infer $R_{\mathrm{sh}} \approx 1.4 \times 10^{10}$ cm. However, such a small radius is inconsistent with the high Lorentz factor and $\sim 10^2$ s duration of the outburst since in relativistic expansion the expected radius is $R_{\mathrm{sh}} \approx 4\gamma^2 ct \approx 10^{17}$ cm. We

thus conclude that the relativistic outflow hypothesis is inconsistent with the data. This rules out recent claims[48] that neglected to consider the UV/optical non-detections.

We can also reject a relativistic origin for the outburst based on the later radio observations. The radio data require sub-relativistic ejecta ($\beta \approx 0.25$), which however may have been relativistic initially and rapidly decelerated. In this scenario the shock dynamics are given the Sedov-Taylor self-similar solution. For an initially relativistic outflow with $E_K \sim E_X \approx 2 \times 10^{46}$ erg in a wind circumstellar medium (CSM) [$\rho(r) \propto r^{-2}$] with $A_* \approx 1$, we find that the outflow will become non-relativistic at $t \approx 400$ s. Subsequently, the outflow will evolve according to[49] $R \propto t^{2/3}$, $B \propto t^{-1}$, and $\gamma_m \propto t^{-2/3}$.

The observed radio spectrum peaks at the synchrotron self-absorption frequency, ν_a, and the spectrum at higher frequencies is described by $F_\nu \propto \nu^{-(p-1)/2}$ with $p = 3.2$. From this we infer that in the Sedov-Taylor regime the spectrum evolves as $F_{\nu,a} \propto t^{-1.4}$ and $\nu_a \propto t^{-1.3}$. This leads to $F_\nu \propto t^{1.8}$ for $\nu < \nu_a$ and $F_\nu \propto t^{-2.8}$ for $\nu > \nu_a$. These scalings are clearly inconsistent with the observed $\nu_a \propto t^{-1.1}$ and $F_{\nu,a} \propto t^{-0.4}$, as well as the light curve rise and decay, $F_\nu \propto t^{1.4}$ and $F_\nu \propto t^{-1.2}$, respectively. The failure of this model is tied to the underlying assumption of a single velocity component (relevant for a GRB-like relativistic outflow).

4 SYNOW Fits of the Optical spectra

We compare our Gemini spectroscopic observations of SN 2008D with synthetic spectra made with the supernova spectrum synthesis code SYNOW[50] (Figure 3). SYNOW* is a highly parametrized spectral synthesis code used primarily for empirical analysis of SN spectra. The code is based on simple assumptions: spherical symmetry, homologous expansion, a sharp photosphere that emits a blackbody spectrum, and line formation by resonance scattering treated in the Sobolev approximation. Its main function is to make line identifications and estimate the velocity at the photosphere (Figure 4) and the velocity interval within which each ion is detected. These quantities provide constraints on the composition structure of the ejecta.

*http://www.nhn.ou.edu/∼parrent/synow.html

Here we fit the pre-maximum spectra with power law and Gaussian optical depth profiles for photospheric velocity and high velocity (HV) features, respectively. The synthetic and observed spectra are normalized[51] before fitting. The results obtained show that SN 2008D follows the standard line identification scheme for a typical He-rich Type Ibc supernova.

From 14 to 3 days before maximum light, blue shifted He I and Fe II absorption features indicate photospheric velocities ranging from 17,000 down to 11,500 km s^{-1}, respectively (Figure 3). We note that fits were not possible for the first few epochs due to the nearly featureless spectra with contribution from the cooling envelope component. The spectra also contain O I and it is suspected that if the spectrum extended further into UV and infrared wavelength regions that absorption of Ca II would also be seen. We take the interpretation that the absorption feature near 6150 Å is due to either a HV component of H I or Si II (see Refs. 52 and 53 for a full discussion of the discrepancy of this feature).

5 Supernova Optical Emission Models

To quantitatively extract the parameters of SN 2008D we fit the bolometric light curve with a model of supernova emission powered by the radioactive decay of ^{56}Ni and ^{56}Ni+^{56}Co, combined with blackbody emission from the cooling stellar envelope (Figure 5). The ^{56}Ni+^{56}Co model assumes perfect trapping of the photons generated by the ^{56}Co decay, but a comparison to other SNe indicates that some diffusion is likely to occur. The observed evolution is therefore expected to be bounded by the two models, consistent with our latest optical measurements (Figure 5).

The SN models make the following assumptions[61]: homologous expansion, spherical symmetry, no nickel mixing, a constant optical opacity, optically thick ejecta, and ^{56}Ni (or ^{56}Ni+^{56}Co) as the only energy source. With these assumptions the luminosity is given by: $L(t) = M_{\rm Ni}\, e^{-x^2} \times \left[(\epsilon_{\rm Ni} - \epsilon_{\rm Co}) \int_0^x 2ze^{z^2-2xy}dz + \epsilon_{\rm Co} \int_0^x 2ze^{z^2-2xy+2zs}dz\right]$, where $x \equiv t/\tau_m$, $y \equiv \tau_m/2\tau_{\rm Ni}$, $s \equiv \tau_m(\tau_{\rm Co} - \tau_{\rm Ni})/2\tau_{\rm Co}\tau_{\rm Ni}$, $\epsilon_{\rm Ni} = 3.9 \times 10^{10}$ erg s^{-1} g^{-1}, $\epsilon_{\rm Co} = 6.8 \times 10^9$ erg s^{-1} g^{-1}, $\tau_{\rm Ni} = 8.8$ d, and $\tau_{\rm Co} = 111.3$ d. In the ^{56}Ni model only the first term on the right hand side is used, with a prefactor of $\epsilon_{\rm Ni}$. The light curve timescale is given by $\tau_m = 0.36(\kappa^2 M_{\rm ej}^3/c^2 E_K)^{1/4}$, where $\kappa \approx 0.05$ is the optical opacity. Thus, the peak of the

light curve is determined by $M_{\rm Ni}$, while the time of the peak (and hence the width of the light curve) is determined by the ratio of $M_{\rm ej}$ to E_K.

In the ^{56}Ni model we find that the best fit model has $M_{\rm Ni} \approx 0.1$ M$_\odot$ and $\tau_m \approx 23$ d. In the ^{56}Ni+^{56}Co model we find $M_{\rm Ni} \approx 0.05$ M$_\odot$ and $\tau_m \approx 15$ d. To break the degeneracy between E_K and $M_{\rm ej}$ we use the photospheric velocity, $v_{\rm ph} = (10E_K/3M_{\rm ej})^{1/2}(1 - 9.3E_K t^2/\kappa M_{\rm ej}^2)$, which is measured at maximum light ($t \approx 20$ d) to be $11,500$ km s^{-1}. From the measured τ_m and using $\kappa = 0.05$ we find $M_{\rm ej}^{3/4} E_K^{-1/4} \approx 3 \times 10^{12}$ (^{56}Ni+^{56}Co model) or $\approx 4 \times 10^{12}$ (^{56}Ni model). With these values the second term in the equation for $v_{\rm ph}$ provides a $\lesssim 5\%$ correction, so $E_K/M_{\rm ej} \approx 4.0 \times 10^{17}$ erg g^{-1}. For self-consistency we use the inferred values of $M_{\rm ej}$ and E_K as the input parameters to the envelope cooling model. We find that we need to correct these values by about 30% to provide a satisfactory combined fit. This is remarkable agreement considering the various simplifications that enter both models.

6 The X-ray light curve of XRO 080109/SN 2008D

We obtained X-ray observations with the ACIS-S instrument on-board the Chandra X-ray Observatory on Jan 19.86 UT (10.3 days after the outburst). In the 17.9 ks observation we detect a weak point source coincident with the radio position of XRO 080109. The data were reduced and the source counts were extracted in the standard manner using the Chandra threads. A total of 10 counts were found in a 4.9 arcsec aperture, corresponding to a count rate of 5.6×10^{-4} counts s^{-1}. The low count rate precludes a constrained spectral fit, and we therefore adopt the parameters of the X-ray outburst (Figure 1).

We fit the normalization of the spectrum using `xspec` v11.3.2 and determine an unabsorbed flux, $F_X = (1.2 \pm 0.4) \times 10^{-14}$ erg cm^{-2} s^{-1} ($0.3 - 10$ keV). The high angular resolution of the image reveals three sources near the position of XRO 080109, which are located within the 18 arcsec Point Spread Function (PSF) of XRT and therefore contaminate the late XRT observations (Figure 6). To remove this contamination we use the positions, count rates, and spectra of the three sources in `xspec` to determine their equivalent XRT count rates. Using the software package Sherpa, the XRT PSF profiles for the three sources were calculated at the XRT count rates and CXO positions. We then

measure the combined contamination at the position of XRO 080109, and use a small (4 arcsec) aperture to correctly extract the X-ray flux in all XRT observation after 0.1 days (Figure 7).

7 The Luminosity, Star Formation Rate, and Metallicity of NGC 2770

We determine the properties of NGC 2770 using optical observations from the Sloan Digital Sky Survey (SDSS), near-IR data from the Two Micron All Sky Survey (2MASS), far-IR data from the Infrared Astronomical Satellite (IRAS), and radio data from the VLA. The broad-band spectral energy distribution (SED) is shown in Figure 8. Using the SDSS photometry we infer[55] a luminosity of 0.3 L_*. The SDSS u-band luminosity of 3.5×10^{27} erg s^{-1} Hz^{-1}, corresponds[56] to an unobscured star formation rate, SFR ≈ 0.5 M$_\odot$ yr^{-1}.

In addition, NGC 2770 is detected at decimeter and far-IR (FIR) wavelengths, which are sensitive to obscured star formation activity. We find an integrated 20-cm flux of 17.8 ± 1.8 mJy, corresponding[57] to SFR ≈ 0.6 M$_\odot$ yr^{-1}. The far-IR luminosity as inferred from detections with the Infrared Astronomical Satellite ($12 - 100$ μm) is $L_{\rm FIR} \approx 10^{10}$ L$_\odot$, corresponding[56] to SFR ≈ 0.9 M$_\odot$ yr^{-1}. Thus, all three star formation indicators lead to a rate of about $0.5 - 1$ M$_\odot$ yr^{-1}, with at most 50% obscured star formation. This is a modest star formation rate, which normalized by luminosity is roughly similar to that in the Milky Way galaxy.

As shown in Figure 8, NGC 2770 is consistent with a typical spiral galaxy (Sb/Sc) template, but is at least two orders of magnitude less luminous in the far-IR band than the extreme starburst galaxy Arp 220. This indicates that the elevated core-collapse SN rate in NGC 2770 is not due to on-going starburst activity, as in Arp 220 (with an inferred SN rate of 4 ± 2 yr^{-1}).

We next investigate the metallicity of NGC 2770 in the context of a comparison to the metallicities of GRB-SNe host galaxies. To this end, we obtained two 1200 s spectra with the Dual Imaging Spectrograph on the Astrophysical Research Consortium 3.5-m telescope at Apache Point Observatory. We used a 300 l/mm grating in the wavelength range 5930-8700 Å (dispersion of 2.3 Å/pix) and a 400 l/mm grating in the wavelength range 3450-5640 Å (dispersion of 1.8 Å/pix). The 1.5 arcsec wide slit was aligned along

the major axis of the galaxy (corresponding to a position angle of $-30°$). The spectra were reduced using standard packages in IRAF. Flux calibration was achieved with the spectrophotometric standard star Feige 34.

The reduced spectrum covers the full visible extent of NGC 2770, a semi-major axis of about 9 kpc. We detect several bright HII regions along the slit, which produce bright emission lines of hydrogen, oxygen, nitrogen, and sulfur. The profiles of the Hα and [NII] emission lines along the major axis of the galaxy are shown in Figure 9. Using the full complement of detected lines we simultaneously infer[58] the ionization parameter and metallicity of the various HII regions. The ionization parameter is relatively uniform with a value of $10^{7.4\pm0.2}$ cm s^{-1}. The metallicity as a function of galactocentric radius exhibits a shallow gradient with a central metallicity of $12 + \log(\mathrm{O/H}) \approx 9.1$ or about 1.5 $\mathrm{Z}_\odot$. At $3 - 8$ kpc the metallicity is about 0.6 $\mathrm{Z}_\odot$, and near the position of XRO 080109 it is about 0.5 $\mathrm{Z}_\odot$. A comparison to the luminosity-metallicity relation from SDSS[59] indicates that NGC 2770 is located along the relation.

It has been recently argued[60] that the host galaxies of long GRBs are preferentially low metallicity and luminosity systems, with $12 + \log(\mathrm{O/H}) \approx 7.9 - 8.6$ and $M_B \approx -15.9$ to -19.3 mag. Clearly, NGC 2770 has a higher luminosity and metallicity than these host galaxies, although we note that with the shallow gradient the metallicity near the position of XRO 080109 is marginally consistent with those of long GRB hosts.

Received 29 March 2008; Accepted **draft**.

45. Mu]nari, U. & Zwitter, T. Equivalent width of NA I and K I lines and reddening. *Astr. Astrophys.* **318**, 269–274 (1997).

46. Cardelli, J. A., Clayton, G. C. & Mathis, J. S. The relationship between infrared, optical, and ultraviolet extinction. *Astrophys. J.* **345**, 245–256 (1989).

47. Sari, R., Piran, T. & Narayan, R. Spectra and Light Curves of Gamma-Ray Burst Afterglows. *Astrophys. J. Lett.* **497**, L17+ (1998).

48. Xu, D., Zou, Y.-C. & Fan, Y.-Z. Mildly relativistic X-ray transient 080109 and SN2008D: Towards a continuum from energetic GRB/XRF to ordinary Ibc SN. *ArXiv e-prints* **801**, 1+ (2008).

49. Waxman, E. The Nature of GRB 980425 and the Search for Off-Axis Gamma-Ray Burst Signatures in Nearby Type Ib/c Supernova Emission. *Astrophys. J.* **602**, 886–891 (2004).

50. Branch, D., Parrent, J., Troxel, M. A., Casebeer, D., Jeffery, D. J. *et al.* in *American Institute of Physics Conference Series* 342–349 (2007).

51. Jeffery, D. J., Ketchum, W., Branch, D., Baron, E., Elmhamdi, A. *et al.* Goodness-of-Fit Tests DIFF1 and DIFF2 for Locally Normalized Supernova Spectra. *Astrophys. J. Suppl.* **171**, 493–511 (2007).

52. Branch, D., Benetti, S., Kasen, D., Baron, E., Jeffery, D. J. *et al.* Direct Analysis of Spectra of Type Ib Supernovae. *Astrophys. J.* **566**, 1005–1017 (2002).

53. Parrent, J., Branch, D., Troxel, M. A., Casebeer, D., Jeffery, D. J. *et al.* Direct Analysis of Spectra of the Unusual Type Ib Supernova 2005bf. *Publ. Astr. Soc. Pacific* **119**, 135–142 (2007).

54. Pian, E., Mazzali, P. A., Masetti, N., Ferrero, P., Klose, S. *et al.* An optical supernova associated with the X-ray flash XRF 060218. *Nature* **442**, 1011–1013 (2006).

55. Blanton, M. R., Hogg, D. W., Bahcall, N. A., Brinkmann, J., Britton, M. *et al.* The Galaxy Luminosity Function and Luminosity Density at Redshift z = 0.1. *Astrophys. J.* **592**, 819–838 (2003).

56. Kennicutt, Jr., R. C. Star Formation in Galaxies Along the Hubble Sequence. *Ann. Rev. Astr. Ap.* **36**, 189–232 (1998).

57. Yun, M. S. & Carilli, C. L. Radio-to-Far-Infrared Spectral Energy Distribution and Photometric Redshifts for Dusty Starburst Galaxies. *Astrophys. J.* **568**, 88–98 (2002).

58. Kewley, L. J. & Dopita, M. A. Using Strong Lines to Estimate Abundances in Extragalactic H II Regions and Starburst Galaxies. *Astrophys. J.* **142**, 35–52 (2002).

59. Tremonti, C. A., Heckman, T. M., Kauffmann, G., Brinchmann, J., Charlot, S. *et al.* The Origin of the Mass-Metallicity Relation: Insights from 53,000 Star-forming Galaxies in the Sloan Digital Sky Survey. *Astrophys. J.* **613**, 898–913 (2004).

60. Stanek, K. Z., Gnedin, O. Y., Beacom, J. F., Gould, A. P., Johnson, J. A. *et al.* Protecting Life in the Milky Way: Metals Keep the GRBs Away. *Acta Astronomica* **56**, 333–345 (2006).

61. Arnett, W. D. Type I supernovae. I - Analytic solutions for the early part of the light curve. *Astrophys. J.* **253**, 785–797 (1982).

62. Alard, C. & Lupton, R. H. A Method for Optimal Image Subtraction *Astrophys. J.* **503**, 325–331 (1998).

63. Cenko, S. B., Fox, D. W., Moon, D.-S., Harrison, F. A., Kulkarni, S. R. *et al.* The Automated Palomar 60 Inch Telescope *Astrophys. J.* **118**, 1398-1406 (2006).

Δt (sec)	Bin Width (sec)	Unabsorbed Flux (erg cm^{-2} s^{-1})	Flux Error (erg cm^{-2} s^{-1})
29.009995	15.000000	2.61×10^{-10}	5.1×10^{-11}
54.009995	10.000000	4.38×10^{-10}	8.1×10^{-11}
69.009995	5.0000000	6.94×10^{-10}	1.4×10^{-10}
79.009995	5.0000000	6.94×10^{-10}	1.4×10^{-10}
91.510010	7.5000076	6.04×10^{-10}	1.1×10^{-10}
106.51001	7.5000000	4.83×10^{-10}	9.8×10^{-11}
121.51001	7.5000000	5.84×10^{-10}	1.0×10^{-10}
134.01001	5.0000000	6.34×10^{-10}	1.3×10^{-10}
146.51001	7.5000000	4.43×10^{-10}	9.4×10^{-11}
166.51001	12.500000	2.90×10^{-10}	5.9×10^{-11}
189.01001	10.000000	3.01×10^{-10}	6.7×10^{-11}
209.01001	10.000000	3.77×10^{-10}	7.5×10^{-11}
231.51001	12.500000	2.41×10^{-10}	5.4×10^{-11}
264.01001	20.000000	1.50×10^{-10}	3.3×10^{-11}
299.01001	15.000000	2.01×10^{-10}	4.5×10^{-11}
336.51001	17.500000	1.03×10^{-10}	2.9×10^{-11}
374.01001	20.000000	1.12×10^{-10}	2.9×10^{-11}
424.01001	30.000000	6.04×10^{-11}	1.7×10^{-11}
529.01001	75.000000	2.61×10^{-11}	7.2×10^{-12}
759.01001	155.00000	1.16×10^{-11}	3.3×10^{-12}
14953.111	9184.4981	2.04×10^{-13}	1.0×10^{-13}
815541.60	682047.40	1.94×10^{-14}	8.7×10^{-15}
2708958.41	1177385.41	$\lesssim 5.12\times10^{-14}$	—

Table 1. Summary of *Swift*/XRT measurements (0.3-10 keV) of XRO 080109/SN 2008D. Time is measured since the derived explosion date, 2008 Jan 9.56 UT.

Date (UT)	Δt (days)	Exposure (s)	Telescope/Inst.
Jan 11.36	1.80	1200	Gemini/GMOS
Jan 12.51	2.95	1500	Gemini/GMOS
Jan 13.49	3.93	2400	Gemini/GMOS
Jan 14.46	4.90	2400	Gemini/GMOS
Jan 15.48	5.92	1500	Gemini/GMOS
Jan 16.49	6.93	1500	Gemini/GMOS
Jan 17.44	7.88	1500	Gemini/GMOS
Jan 18.35	8.79	1500	Gemini/GMOS
Jan 18.52	8.96	2400	APO 3.5m/DIS
Jan 19.50	9.94	1500	Gemini/GMOS
Jan 22.50	12.94	1500	Gemini/GMOS
Jan 25.47	15.91	1500	Gemini/GMOS
Jan 30.20	20.66	2400	APO 3.5m/DIS
Jan 30.60	21.04	1500	Gemini/GMOS
Jan 31.40	21.84	2×900	P200/DBSP
Feb 1.31	22.75	2×900	P200/DBSP
Feb 7.28	28.7	2×1500	P200/DBSP
Feb 9.39	30.83	1200	HET
Feb 11.37	32.81	1200	HET
Feb 11.38	32.82	1550	Gemini/GMOS
Feb 12.23	33.67	2400	HET
Feb 15.44	36.88	1500	Gemini/GMOS
Feb 19.38	40.82	2100	Gemini/GMOS
Feb 22.40	43.84	3600	APO 3.5m/DIS
Feb 23.41	44.85	2400	Gemini/GMOS
Feb 25.11	46.55	2400	HET
Feb 27.12	48.56	2400	HET
Feb 27.39	48.83	2400	Gemini/GMOS
Mar 1.36	51.80	1800	Gemini/GMOS
Mar 2.10	52.54	2400	HET
Mar 6.35	56.79	2100	Gemini/GMOS

Table 2. Summary of Spectroscopic Observations of XRO 080109/SN 2008D.

Mid-Exposure Time (UT)	Bin Width (s)	Filter	m (Vega mag)	$\sigma(m)$ (Vega mag)	F_ν (erg cm^{-2} s^{-1} Hz^{-1})	$\sigma(F_\nu)$ (erg cm^{-2} s^{-1} Hz^{-1})
2008-01-09 17:09:33.9	8854	UVW2	20.52	+0.44/−0.31	4.581×10^{-29}	1.516×10^{-29}
2008-01-11 06:09:10.1	14292	UVW2	$\gtrsim 20.96$	—	$\lesssim 3.054\times10^{-29}$	—
2008-01-11 16:29:13.4	17980	UVW2	$\gtrsim 21.40$	—	$\lesssim 2.083\times10^{-29}$	—
2008-01-12 05:15:50.1	22752	UVW2	$\gtrsim 20.96$	—	$\lesssim 3.183\times10^{-29}$	—
2008-01-12 20:39:58.8	26900	UVW2	$\gtrsim 21.16$	—	$\lesssim 2.545\times10^{-29}$	—
2008-01-13 15:17:24.3	34483	UVW2	$\gtrsim 21.27$	—	$\lesssim 2.233\times10^{-29}$	—
2008-01-14 14:31:44.9	43473	UVW2	$\gtrsim 21.40$	—	$\lesssim 2.060\times10^{-29}$	—
2008-01-15 18:34:22.3	51660	UVW2	$\gtrsim 21.40$	—	$\lesssim 1.927\times10^{-29}$	—
2008-01-16 16:56:27.4	23324	UVW2	$\gtrsim 20.96$	—	$\lesssim 3.159\times10^{-29}$	—
2008-01-18 22:02:20.0	80486	UVW2	$\gtrsim 21.71$	—	$\lesssim 1.456\times10^{-29}$	—
2008-01-20 05:55:48.4	29168	UVW2	$\gtrsim 21.40$	—	$\lesssim 2.034\times10^{-29}$	—
2008-01-09 17:16:38.3	8790	UVM2	$\gtrsim 20.11$	—	$\lesssim 6.621\times10^{-29}$	—
2008-01-11 06:21:49.2	14501	UVM2	20.34	+0.42/−0.30	5.535×10^{-29}	1.774×10^{-29}
2008-01-11 16:45:26.4	17741	UVM2	20.48	+0.27/−0.22	4.839×10^{-29}	1.069×10^{-29}
2008-01-12 05:24:13.1	22437	UVM2	$\gtrsim 20.43$	—	$\lesssim 5.259\times10^{-29}$	—
2008-01-12 20:47:17.5	26680	UVM2	$\gtrsim 20.74$	—	$\lesssim 3.714\times10^{-29}$	—
2008-01-13 15:22:23.6	34547	UVM2	$\gtrsim 20.86$	—	$\lesssim 3.288\times10^{-29}$	—
2008-01-14 14:36:39.7	43443	UVM2	$\gtrsim 21.01$	—	$\lesssim 2.945\times10^{-29}$	—
2008-01-15 18:39:52.4	51639	UVM2	$\gtrsim 20.86$	—	$\lesssim 3.252\times10^{-29}$	—
2008-01-16 17:01:42.5	23228	UVM2	$\gtrsim 20.52$	—	$\lesssim 4.758\times10^{-29}$	—
2008-01-18 22:12:21.2	80708	UVM2	$\gtrsim 21.62$	—	$\lesssim 1.813\times10^{-29}$	—
2008-01-20 06:09:58.3	29129	UVM2	$\gtrsim 21.18$	—	$\lesssim 2.353\times10^{-29}$	—
2008-01-09 17:03:50.9	8782	UVW1	20.12	+0.43/−0.31	8.193×10^{-29}	2.681×10^{-29}
2008-01-11 05:57:31.1	13897	UVW1	20.01	+0.20/−0.17	9.047×10^{-29}	1.535×10^{-29}
2008-01-11 16:15:35.7	17832	UVW1	19.69	+0.13/−0.12	1.222×10^{-28}	1.368×10^{-29}
2008-01-12 05:10:10.5	22861	UVW1	20.33	+0.34/−0.26	6.795×10^{-29}	1.829×10^{-29}
2008-01-12 20:34:50.3	26948	UVW1	$\gtrsim 20.78$	—	$\lesssim 4.428\times10^{-29}$	—

2008-01-13 15:12:46.4	34337	UVW1	$\gtrsim 20.93$	—	$\lesssim 3.915 \times 10^{-29}$	—
2008-01-14 14:27:39.0	43407	UVW1	$\gtrsim 21.01$	—	$\lesssim 3.648 \times 10^{-29}$	—
2008-01-15 18:29:42.2	51576	UVW1	$\gtrsim 22.12$	—	$\lesssim 3.780 \times 10^{-29}$	—
2008-01-17 04:08:33.3	63877	UVW1	$\gtrsim 21.68$	—	$\lesssim 1.982 \times 10^{-29}$	—
2008-01-18 10:45:45.7	40881	UVW1	$\gtrsim 21.01$	—	$\lesssim 3.639 \times 10^{-29}$	—
2008-01-21 04:21:47.1	46692	UVW1	$\gtrsim 21.68$	—	$\lesssim 2.045 \times 10^{-29}$	—
2008-01-26 04:03:58.5	141936	UVW1	$\gtrsim 22.29$	—	$\lesssim 1.172 \times 10^{-29}$	—
2008-01-28 21:53:24.3	89869	UVW1	$\gtrsim 21.85$	—	$\lesssim 1.662 \times 10^{-29}$	—
2008-02-03 08:05:44.8	170423	UVW1	$\gtrsim 21.54$	—	$\lesssim 2.105 \times 10^{-29}$	—
2008-02-09 08:37:03.1	20536	UVW1	$\gtrsim 21.41$	—	$\lesssim 2.614 \times 10^{-29}$	—
2008-01-09 17:06:42.2	8736	U	19.76	$+0.32/-0.25$	1.804×10^{-28}	4.574×10^{-29}
2008-01-11 06:02:19.0	13941	U	18.41	$+0.06/-0.06$	6.274×10^{-28}	3.472×10^{-29}
2008-01-11 16:22:33.9	17705	U	18.47	$+0.05/-0.05$	5.923×10^{-28}	2.677×10^{-29}
2008-01-12 05:13:46.1	22714	U	18.80	$+0.09/-0.09$	4.369×10^{-28}	3.594×10^{-29}
2008-01-12 20:37:53.5	26843	U	19.03	$+0.10/-0.09$	3.530×10^{-28}	3.034×10^{-29}
2008-01-13 15:14:42.1	34350	U	19.23	$+0.10/-0.09$	2.946×10^{-28}	2.605×10^{-29}
2008-01-14 14:29:36.3	43383	U	19.22	$+0.09/-0.08$	2.963×10^{-28}	2.381×10^{-29}
2008-01-15 18:31:54.0	51554	U	19.21	$+0.10/-0.09$	2.980×10^{-28}	2.507×10^{-29}
2008-01-17 04:15:41.5	64125	U	19.11	$+0.05/-0.05$	3.286×10^{-28}	1.450×10^{-29}
2008-01-18 10:52:30.4	41083	U	19.10	$+0.09/-0.09$	3.295×10^{-28}	2.733×10^{-29}
2008-01-21 04:37:19.7	46428	U	18.93	$+0.05/-0.05$	3.860×10^{-28}	1.676×10^{-29}
2008-01-26 04:16:48.4	141673	U	18.92	$+0.03/-0.02$	3.904×10^{-28}	9.028×10^{-30}
2008-01-29 12:32:36.2	141678	U	19.03	$+0.03/-0.03$	3.541×10^{-28}	1.065×10^{-29}
2008-02-02 22:38:19.0	135684	U	19.40	$+0.05/-0.05$	2.500×10^{-28}	1.107×10^{-29}
2008-02-10 12:04:17.9	193928	U	20.30	$+0.12/-0.11$	1.094×10^{-28}	1.159×10^{-29}
2008-02-16 03:52:30.2	99075	U	20.43	$+0.13/-0.12$	9.726×10^{-29}	1.089×10^{-29}
2008-02-23 06:04:01.3	12053	U	20.45	$+0.16/-0.14$	9.541×10^{-29}	1.313×10^{-29}
2008-01-09 17:08:09.3	8733	B	$\gtrsim 20.45$	—	$\lesssim 2.649 \times 10^{-28}$	—
2008-01-11 06:04:59.5	14002	B	19.01	$+0.07/-0.07$	1.007×10^{-27}	6.708×10^{-29}
2008-01-11 16:26:02.9	17692	B	19.11	$+0.06/-0.06$	9.174×10^{-28}	4.878×10^{-29}

2008-01-12 05:15:24.1	22664	B	19.29	$+0.10/-0.09$	7.800×10^{-28}	6.797×10^{-29}
2008-01-12 20:39:19.0	26811	B	19.30	$+0.09/-0.08$	7.739×10^{-28}	5.889×10^{-29}
2008-01-13 15:15:47.1	34371	B	19.39	$+0.08/-0.08$	7.096×10^{-28}	5.183×10^{-29}
2008-01-14 14:30:38.7	43386	B	19.27	$+0.07/-0.06$	7.915×10^{-28}	4.806×10^{-29}
2008-01-15 18:33:04.0	51559	B	19.20	$+0.07/-0.06$	8.462×10^{-28}	5.092×10^{-29}
2008-01-17 04:18:45.3	64234	B	18.98	$+0.04/-0.04$	1.040×10^{-27}	3.945×10^{-29}
2008-01-18 10:55:21.9	41174	B	18.82	$+0.08/-0.07$	1.203×10^{-27}	8.134×10^{-29}
2008-01-21 04:43:40.2	46344	B	18.58	$+0.04/-0.04$	1.506×10^{-27}	5.279×10^{-29}
2008-01-26 04:22:01.8	141589	B	18.50	$+0.02/-0.02$	1.607×10^{-27}	2.781×10^{-29}
2008-01-29 12:38:08.9	141650	B	18.56	$+0.02/-0.02$	1.528×10^{-27}	3.052×10^{-29}
2008-02-02 22:44:12.4	135760	B	18.75	$+0.03/-0.02$	1.287×10^{-27}	2.963×10^{-29}
2008-02-10 12:54:34.9	191010	B	19.66	$+0.06/-0.06$	5.549×10^{-28}	2.950×10^{-29}
2008-02-18 03:16:32.0	269426	B	20.25	$+0.08/-0.07$	3.220×10^{-28}	2.254×10^{-29}
2008-02-23 11:48:17.2	2977	B	21.01	$+0.66/-0.41$	$\lesssim 2.170\times10^{-28}$	—
2008-01-09 17:15:14.4	8721	V	$\gtrsim 19.66$	—	$\lesssim 4.98\times10^{-28}$	—
2008-01-11 06:18:10.0	14302	V	18.38	$+0.10/-0.09$	1.625×10^{-27}	1.461×10^{-28}
2008-01-11 16:43:11.8	17629	V	18.41	$+0.07/-0.06$	1.573×10^{-27}	9.493×10^{-29}
2008-01-12 05:23:24.1	22413	V	18.50	$+0.12/-0.11$	1.454×10^{-27}	1.532×10^{-28}
2008-01-12 20:46:18.5	26648	V	18.52	$+0.09/-0.09$	1.431×10^{-27}	1.170×10^{-28}
2008-01-13 15:21:00.1	34478	V	18.42	$+0.08/-0.07$	1.555×10^{-27}	1.053×10^{-28}
2008-01-14 14:35:34.7	43398	V	18.27	$+0.06/-0.06$	1.786×10^{-27}	9.862×10^{-29}
2008-01-15 18:38:40.0	51585	V	18.11	$+0.06/-0.05$	2.071×10^{-27}	1.069×10^{-28}
2008-01-17 04:23:21.6	64148	V	17.93	$+0.04/-0.04$	2.451×10^{-27}	9.093×10^{-29}
2008-01-19 18:14:22.2	83914	V	17.82	$+0.06/-0.06$	2.724×10^{-27}	1.513×10^{-28}
2008-01-21 12:00:20.0	20316	V	17.48	$+0.05/-0.04$	3.698×10^{-27}	1.550×10^{-28}
2008-01-26 04:24:40.7	141566	V	17.41	$+0.02/-0.02$	3.970×10^{-27}	6.771×10^{-29}
2008-01-29 12:33:46.8	141227	V	17.41	$+0.02/-0.02$	3.966×10^{-27}	6.891×10^{-29}
2008-02-02 22:38:00.5	135243	V	17.50	$+0.02/-0.02$	3.645×10^{-27}	6.528×10^{-29}
2008-02-10 11:58:41.7	194144	V	17.96	$+0.03/-0.03$	2.380×10^{-27}	6.056×10^{-29}
2008-02-18 03:05:35.5	269360	V	18.37	$+0.03/-0.03$	1.633×10^{-27}	4.748×10^{-29}

2008-02-24 16:01:14.1	104764	V	18.68	$+0.07/-0.06$	1.231×10^{-27}	7.343×10^{-29}
2008-03-12 13:53:04.6	3538	V	19.03	$+0.08/-0.08$	8.926×10^{-28}	6.714×10^{-29}

Table 3: Summary of *Swift*/UVOT Observations of XRO 080109/SN 2008D. Magnitudes are not corrected for extinction. All upper limits are 3σ. The UVOT images were reduced using standard packages within the HEASOFT software package. data were reduced using standard packages in IRAF. Utilizing pre-explosion images from 2008 Jan 7 UT, we used the ISIS image subtraction package[62] to eliminate the host galaxy contamination from all UVOT images. The only exception is the UVW2 filter for which we used a deep template image constructed from post-explosion data in which the source is not detected. The early UVOT data are binned to increase the signal-to-noise ratio. The data have not been corrected for host galaxy extinction.

Date (MJD)	g (mag)	$\sigma(g)$ (mag)	r (mag)	$\sigma(r)$ (mag)	i (mag)	$\sigma(i)$ (mag)	z (mag)	$\sigma(z)$ (mag)
54476.38	18.48	0.12	18.00	0.05	17.85	0.05	17.59	0.06
54477.37	18.57	0.08	18.01	0.07	17.86	0.05	17.49	0.07
54478.37	18.78	0.15	18.11	0.15	17.92	0.05	17.61	0.09
54479.32	18.81	0.05	18.18	0.09	17.91	0.05	17.61	0.07
54480.36	18.51	0.08	17.87	0.05	17.67	0.05	17.27	0.10
54481.36	18.49	0.06	17.88	0.11	17.57	0.04	17.15	0.05
54483.35	18.35	0.05	17.55	0.10	17.33	0.05	16.89	0.12
54484.35	18.21	0.09	17.45	0.07	17.22	0.05	16.77	0.05
54485.34	17.94	0.07	17.23	0.05	17.00	0.04	16.56	0.07
54496.32	17.84	0.04	16.96	0.04	16.74	0.04	16.20	0.05
54497.22	17.83	0.05	16.87	0.05	16.67	0.05	16.19	0.05
54502.26	18.07	0.05	17.02	0.05	—	—	16.29	0.05
54504.27	18.11	0.07	17.07	0.06	16.84	0.08	16.28	0.05
54505.27	18.29	0.05	17.17	0.06	16.83	0.04	16.36	0.05
54506.27	18.31	0.04	17.22	0.08	16.89	0.04	16.39	0.08
54507.26	18.41	0.05	17.25	0.06	16.93	0.05	16.43	0.05
54508.26	18.57	0.05	17.31	0.05	16.97	0.03	16.48	0.03
54509.26	18.53	0.05	17.39	0.05	17.04	0.05	16.46	0.05
54512.26	18.83	0.06	17.54	0.04	17.16	0.04	16.62	0.05
54513.22	18.82	0.05	17.56	0.07	17.21	0.06	16.63	0.03
54514.19	—	—	17.71	0.05	17.23	0.05	16.60	0.05
54515.40	—	—	—	—	—	—	16.69	0.08
54522.27	19.29	0.06	17.97	0.06	17.50	0.03	16.90	0.07
54523.26	19.43	0.04	17.96	0.06	17.58	0.06	16.89	0.07
54524.26	19.34	0.10	17.98	0.07	17.57	0.05	16.88	0.06
54525.26	19.34	0.08	17.99	0.07	17.60	0.06	16.95	0.08
54529.26	19.43	0.08	18.15	0.08	17.70	0.06	17.01	0.09
54530.25	19.60	0.07	18.19	0.08	17.78	0.05	16.99	0.08
54531.27	19.55	0.08	18.15	0.09	17.75	0.05	17.11	0.08
54534.23	19.54	0.10	18.35	0.12	17.87	0.07	17.14	0.06
54535.29	19.46	0.10	18.27	0.06	17.88	0.06	17.10	0.06
54536.17	19.55	0.08	18.19	0.10	17.82	0.10	17.04	0.08
54537.23	19.54	0.09	18.28	0.07	17.89	0.08	17.12	0.08
54538.23	19.61	0.08	18.32	0.07	17.91	0.06	17.12	0.10

Table 4. Summary of Palomar 60-inch Imaging Observations of XRO 080109/SN 2008D. Observations of the transient were obtained with the Robotic[63] Palomar 60-inch Telescope. The data were reduced using standard using standard packages within IRAF. Utilizing pre-explosion images from SDSS, we used the ISIS image subtraction package[62] to eliminate the host galaxy contamination from all P60 images. The data have not been corrected for host galaxy extinction.

Date (UT)	g (mag)	$\sigma(g)$ (mag)	r (mag)	$\sigma(r)$ (mag)	i (mag)	$\sigma(i)$ (mag)
Jan 11.34	18.75	0.10	18.13	0.06	—	—
Jan 12.50	—	—	18.19	0.07	—	—
Jan 13.48	—	—	18.18	0.06	—	—
Jan 14.45	—	—	18.16	0.08	—	—
Jan 15.45	18.74	0.08	17.99	0.05	17.73	0.06
Jan 16.49	—	—	17.83	0.05	—	—
Jan 17.43	—	—	17.70	0.06	—	—
Jan 18.43	—	—	17.58	0.06	—	—
Jan 19.49	—	—	17.33	0.04	—	—
Jan 25.46	—	—	17.09	0.05	—	—
Jan 30.58	17.89	0.09	17.02	0.05	16.69	0.06
Feb 11.41	18.60	0.08	17.45	0.05	16.99	0.05
Feb 15.43	19.16	0.09	17.71	0.05	17.18	0.06
Feb 19.37	19.42	0.08	17.91	0.06	17.33	0.06
Feb 23.40	19.55	0.08	18.10	0.06	17.49	0.06
Feb 27.38	19.70	0.08	18.25	0.06	17.64	0.07
Mar 6.34	19.84	0.08	18.41	0.06	17.84	0.06

Table 5. Summary of Gemini/GMOS Imaging Observations of XRO 080109/SN 2008D. Data were reduced using standard tools within the `gemini` package of IRAF. We adopt a background area (annulus) near the transient to correct for the host galaxy contamination. The data have not been corrected for host galaxy extinction.

Date (UT)	Δt (days)	Freq. (GHz)	F_ν (mJy)	$\sigma(F_\nu)$ (mJy)	Config.
Jan 10.18	0.65	8.46	0.033	0.033	VLA
Jan 10.20	0.64	4.86	0.022	0.018	VLA
Jan 10.21	0.65	1.43	0.100	0.102	VLA
Jan 10.21	0.65	22.5	0.020	0.031	VLA
Jan 11.32	1.76	8.46	0.050	0.024	VLA
Jan 11.33	1.77	4.86	0.101	0.039	VLA
Jan 12.54	2.98	22.5	1.038	0.051	VLA
Jan 12.58	3.02	8.46	0.131	0.058	VLA
Jan 12.60	3.04	4.86	0.021	0.032	VLA
Jan 13.29	3.73	8.46	0.111	0.018	VLA
Jan 13.33	3.77	22.5	1.685	0.140	VLA
Jan 13.35	3.79	43.4	2.959	0.568	VLA
Jan 14.14	4.58	15.0	1.137	0.196	VLA
Jan 14.26	4.70	8.46	0.392	0.020	VLA
Jan 14.32	4.76	22.5	2.726	0.048	VLA
Jan 14.36	4.80	43.4	3.505	0.203	VLA
Jan 14.50	4.94	95.0	3.200	0.700	CARMA
Jan 15.25	5.69	22.5	3.248	0.044	VLA
Jan 16.10	6.54	22.5	2.417	0.108	VLA
Jan 16.31	6.75	4.86	0.363	0.032	VLA
Jan 16.33	6.77	8.46	1.288	0.024	VLA
Jan 16.40	6.84	95.0	0.600	0.300	CARMA
Jan 17.36	7.80	43.4	3.267	0.403	VLA
Jan 17.38	7.82	22.5	3.919	0.069	VLA
Jan 17.41	7.85	4.86	0.241	0.028	VLA
Jan 17.42	7.86	8.46	0.984	0.020	VLA
Jan 18.50	8.94	95.0	0.290	0.350	CARMA

Jan 19.30	9.74	43.4	2.707	0.253	VLA
Jan 19.32	9.76	22.5	3.274	0.068	VLA
Jan 20.10	10.54	1.43	0.077	0.084	VLA
Jan 20.14	10.58	15.0	3.554	0.199	VLA
Jan 20.19	10.63	4.86	0.517	0.022	VLA
Jan 20.21	10.65	8.46	1.925	0.029	VLA
Jan 21.16	11.60	8.46	2.741	0.043	VLA
Jan 21.16	11.60	4.86	0.940	0.052	VLA
Jan 21.18	11.62	22.5	2.643	0.041	VLA
Jan 21.19	11.63	43.4	1.086	0.326	VLA
Jan 23.14	13.58	15.0	2.367	0.109	VLA
Jan 23.16	13.60	8.46	2.311	0.047	VLA
Jan 23.16	13.60	4.86	0.836	0.032	VLA
Jan 23.45	13.89	43.4	1.282	0.220	VLA
Jan 23.47	13.91	22.5	2.363	0.064	VLA
Jan 25.16	15.60	15.0	2.060	0.204	VLA
Jan 25.17	15.61	8.46	2.726	0.040	VLA
Jan 25.18	15.62	4.86	1.138	0.032	VLA
Jan 26.56	17.00	22.5	1.686	0.068	VLA
Jan 27.13	17.57	43.4	0.556	0.219	VLA
Jan 27.14	17.58	1.43	0.038	0.114	VLA
Jan 27.15	17.59	22.5	1.241	0.051	VLA
Jan 27.41	17.85	15.0	2.410	0.378	VLA
Jan 27.42	17.86	8.46	2.502	0.043	VLA
Jan 27.43	17.87	4.86	1.336	0.030	VLA
Jan 27.46	17.90	43.4	1.180	0.250	VLA
Jan 27.47	17.91	22.5	1.443	0.099	VLA
Jan 30.28	20.72	43.4	0.380	0.382	VLA
Jan 30.30	20.74	22.5	1.202	0.090	VLA
Jan 30.31	20.75	15.0	2.258	0.388	VLA

Jan 30.32	20.76	8.46	2.216	0.056	VLA
Jan 30.33	20.77	4.86	2.514	0.054	VLA
Feb 1.22	22.66	15.0	2.140	0.351	VLA
Feb 1.17	22.61	22.5	1.034	0.061	VLA
Feb 1.23	22.67	8.46	2.295	0.027	VLA
Feb 1.24	22.68	4.86	2.095	0.038	VLA
Feb 3.17	24.61	43.4	0.000	0.391	VLA
Feb 3.19	24.63	1.43	0.103	0.138	VLA
Feb 3.20	24.64	8.46	1.958	0.048	VLA
Feb 3.21	24.65	4.86	2.137	0.057	VLA
Feb 3.22	24.66	22.5	0.950	0.109	VLA
Feb 8.08	29.52	8.46	1.350	0.080	VLBA
Feb 8.22	29.66	8.46	1.421	0.025	VLA
Feb 8.23	29.67	4.86	1.910	0.080	VLA
Feb 9.32	30.76	1.43	0.378	0.147	VLA
Feb 9.33	30.77	22.5	0.639	0.095	VLA
Feb 9.34	30.78	15.0	0.231	0.132	VLA
Feb 14.22	35.66	1.43	0.283	0.263	VLA
Feb 14.26	35.70	22.5	0.451	0.129	VLA
Feb 14.28	35.72	15.0	0.013	0.135	VLA
Feb 14.29	35.73	8.46	1.140	0.051	VLA
Feb 14.30	35.74	4.86	1.775	0.053	VLA
Feb 21.41	41.85	1.43	0.947	0.235	VLA
Feb 21.43	41.87	8.46	0.941	0.050	VLA
Feb 21.43	41.87	4.86	1.503	0.040	VLA
Feb 24.12	45.56	1.43	0.572	0.195	VLA
Feb 24.14	45.58	22.5	0.256	0.065	VLA
Feb 24.15	45.59	4.86	1.144	0.037	VLA
Feb 24.16	45.60	8.46	0.813	0.033	VLA
Mar 7.10	57.54	1.43	2.966	0.412	VLA

Mar 7.11	57.55	4.86	1.427	0.051	VLA
Mar 7.12	57.56	8.46	0.749	0.030	VLA

Table 6: Radio observations of XRO 080109/SN 2008D. All VLA observations were obtained in the standard continuum mode with 2×50 MHz bands. We used the extragalactic source J0911+338 for phase referencing, and 3C 48 and 3C 287 for flux calibration. The VLA and VLBA data were reduced using standard packages within the Astronomical Image Processing System (AIPS). The data from CARMA were reduced using the MIRIAD software package. The fluxes are determined using a Gaussian profile fit to the point source at the position of XRO 080109.

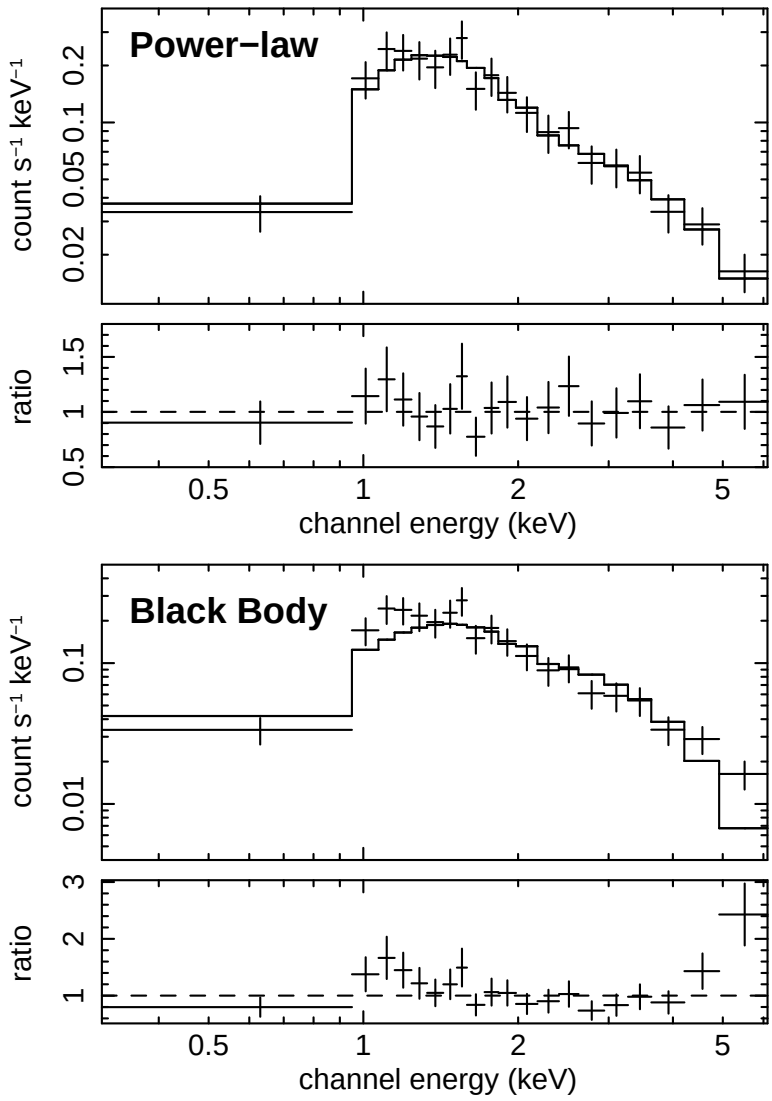

Figure 1. *Swift*/XRT spectrum of the X-ray outburst fit with power-law (top) and blackbody (bottom) models. A comparison of the model residuals (lower panels) reveals that the power-law model provides a better fit to the data.

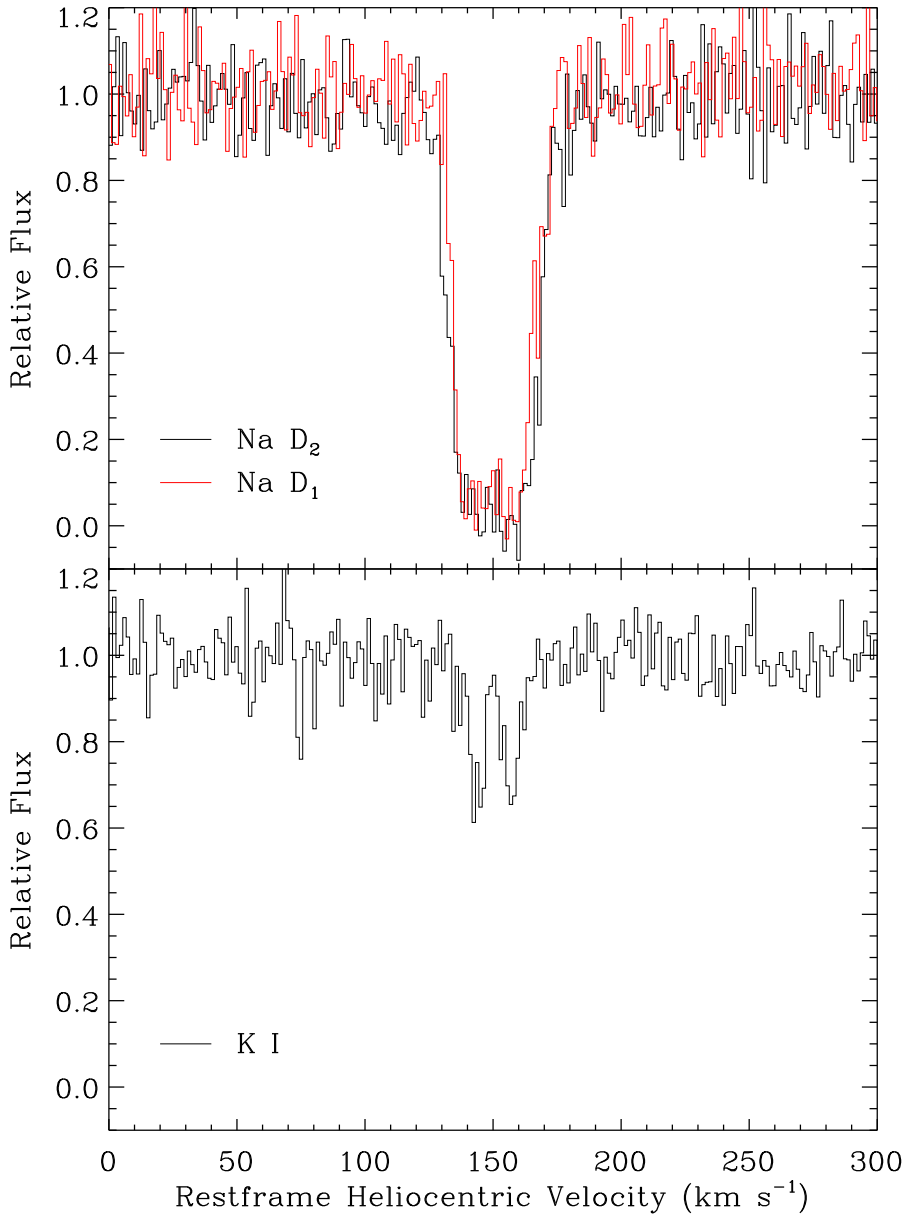

Figure 2. A high resolution spectrum of XRO 080109/SN 2008D centered on the Na I D (top) and K I (bottom) absorption lines. Observations were taken with Keck/HIRES. While the Na I lines are saturated, the K I lines are not, enabling an estimate of the host galaxy extinction.

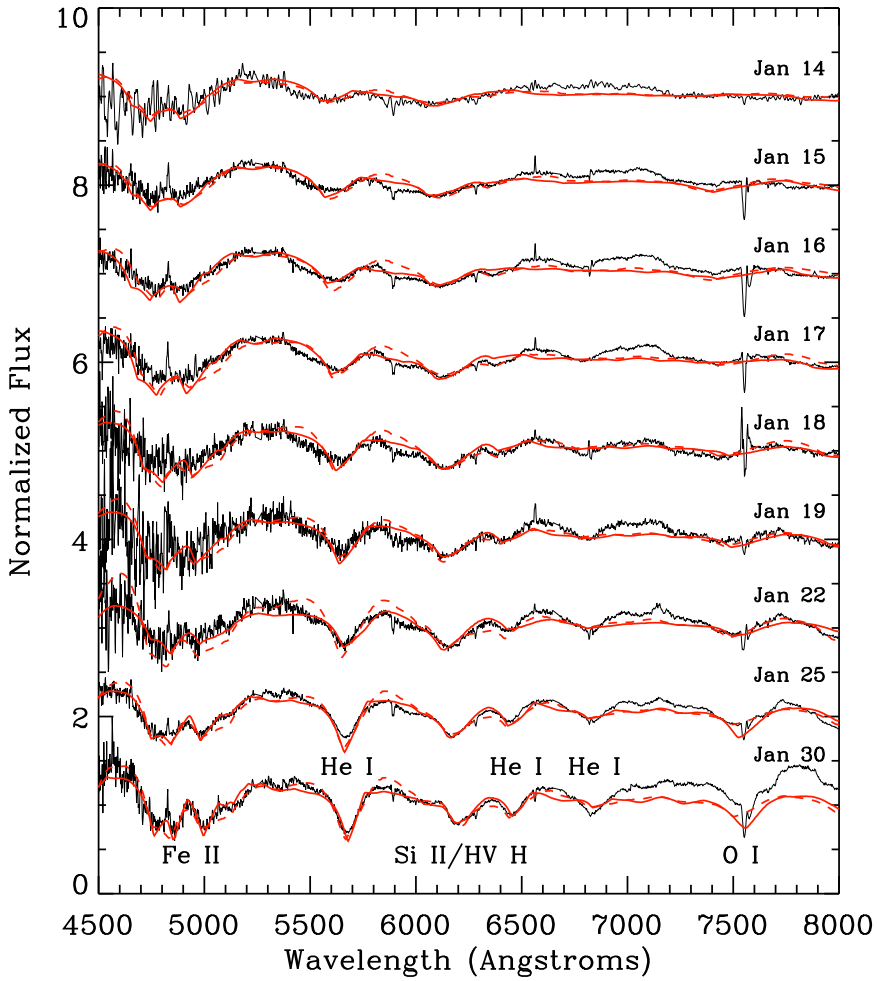

Figure 3. We model our Gemini spectra on multiple nights from 2008 Jan 14 to Jan 30 using spectroscopic fitting code SYNOW. We identify several lines (particularly He I) consistent with a He-rich Type Ibc classification. We additionally find that the feature near 6150 Å is equally well fit with Si II or high velocity hydrogen, similar to the case for SN 2005bf.[53]

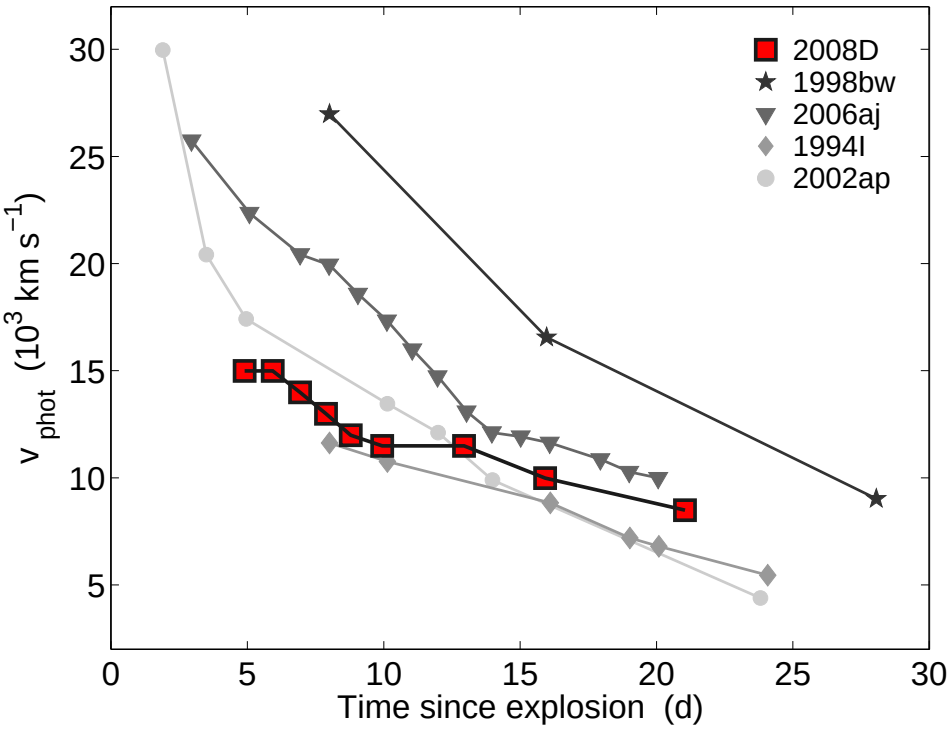

Figure 4. Photospheric velocity as a function of time for SN 2008D. We used the SN fitting code SYNOW to analyze the optical spectra and extract the velocities of the Si II feature at each epoch. The temporal profile of the Si II photospheric velocity is similar to those measured for other SNe Ibc, modeled[54] independently.

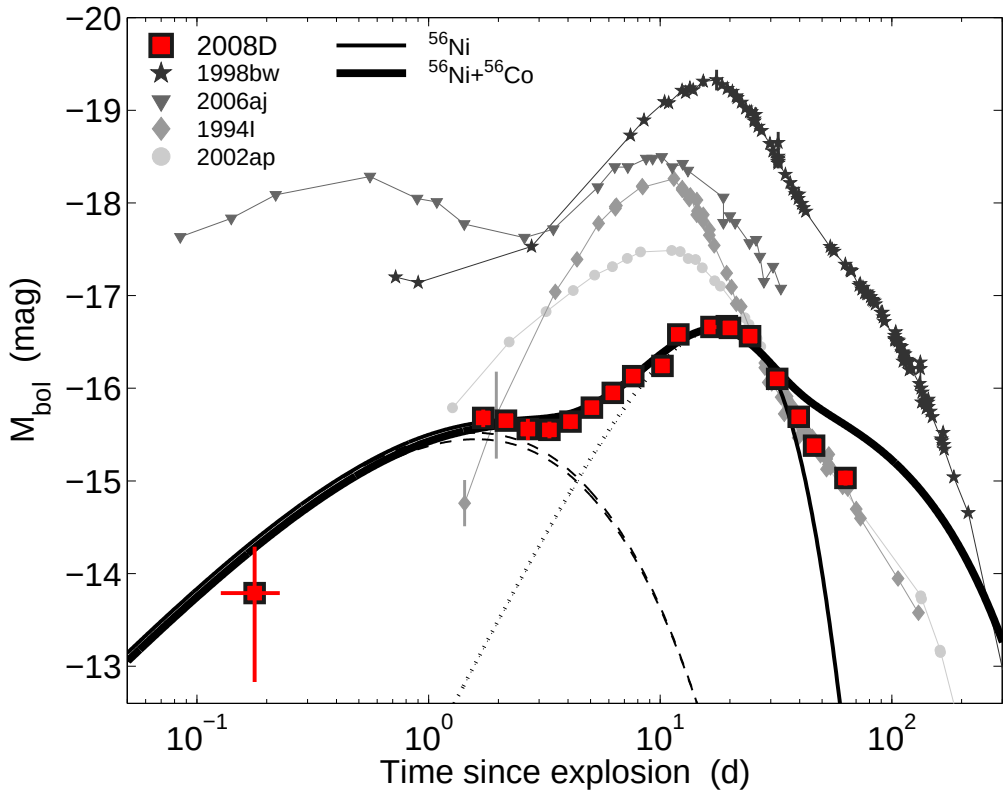

Figure 5. Bolometric magnitude light curve of XRO 080109/SN 2008D. The light curve (red) is constructed using data from UVOT, P60, SLOTIS, and Gemini and are corrected for host galaxy extinction of $A_V = 1.9$ mag. We fit the two light curve components (envelope cooling=dashed lies, SN=dotted lines, sum=solid lines) jointly to determine E_K, $M_{\rm ej}$, and $M_{\rm Ni}$. We use two models for the SN emission, ^{56}Ni (thin line) and ^{56}Ni+^{56}Co (thick line), of which the latter accounts for radiactive decay of ^{56}Co in addition to ^{56}Ni. The observed late-time decay is intermediate between these two models, as expected. Also shown are the light curves of other well-studied SNe Ibc, of which two (1998bw and 2006aj) are associated with sub-energetic GRBs. The light curve of SN 2008D is fainter than the normal SN 2002ap, and peaks at a later time. It is an order of magnitude less luminous than SN 1998bw for which $M_{\rm Ni} \approx 0.5$ M$_\odot$.

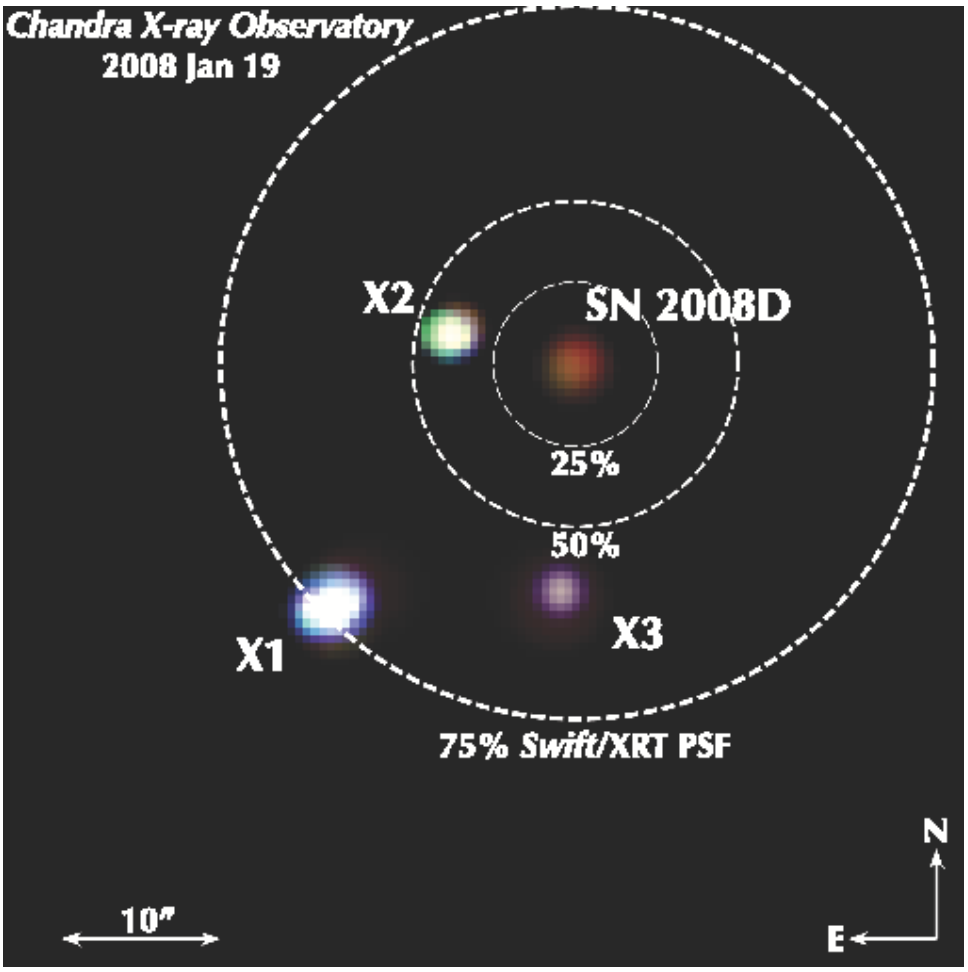

Figure 6. XRO 080109/SN 2008D as observed with CXO on Jan 19.86 UT. The SN is barely detected in the observation (labeled). Three nearby sources are also detected and lie within the PSF of XRT (concentric circles). We note that source "X1" is also visible in the pre-explosion XRT image (Main Article, Figure 1).

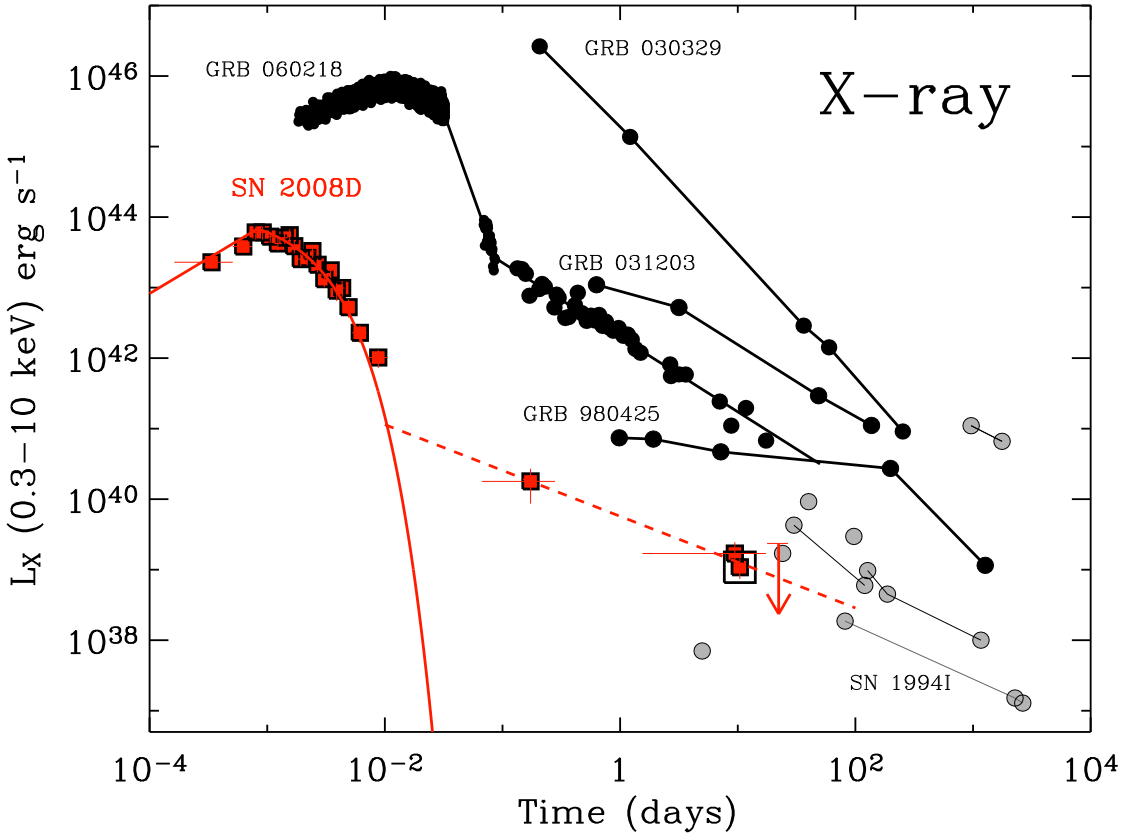

Figure 7. The X-ray light curve of XRO 080109/SN 2008D (red) as observed with XRT (circles) and and CXO (large square) is compared to the afterglows of GRBs 030329, 980425, 031203 and 060218(black, labeled) and other SNe Ibc (grey). The XRT data beyond 0.1 days were corrected for contamination from three nearby source using our CXO observations (Figure 6). The X-ray emission from XRO 080109/SN 2008D is by far the earliest detected from any normal SN Ibc and the luminosity is several orders of magnitude below that of GRBs. An extrapolation of the X-ray decay beyond 0.1 days, $F_X \propto t^{-0.7}$ to the time of typical SN observations indicates a similar luminosity to normal SNe Ibc such as SN 1994I.

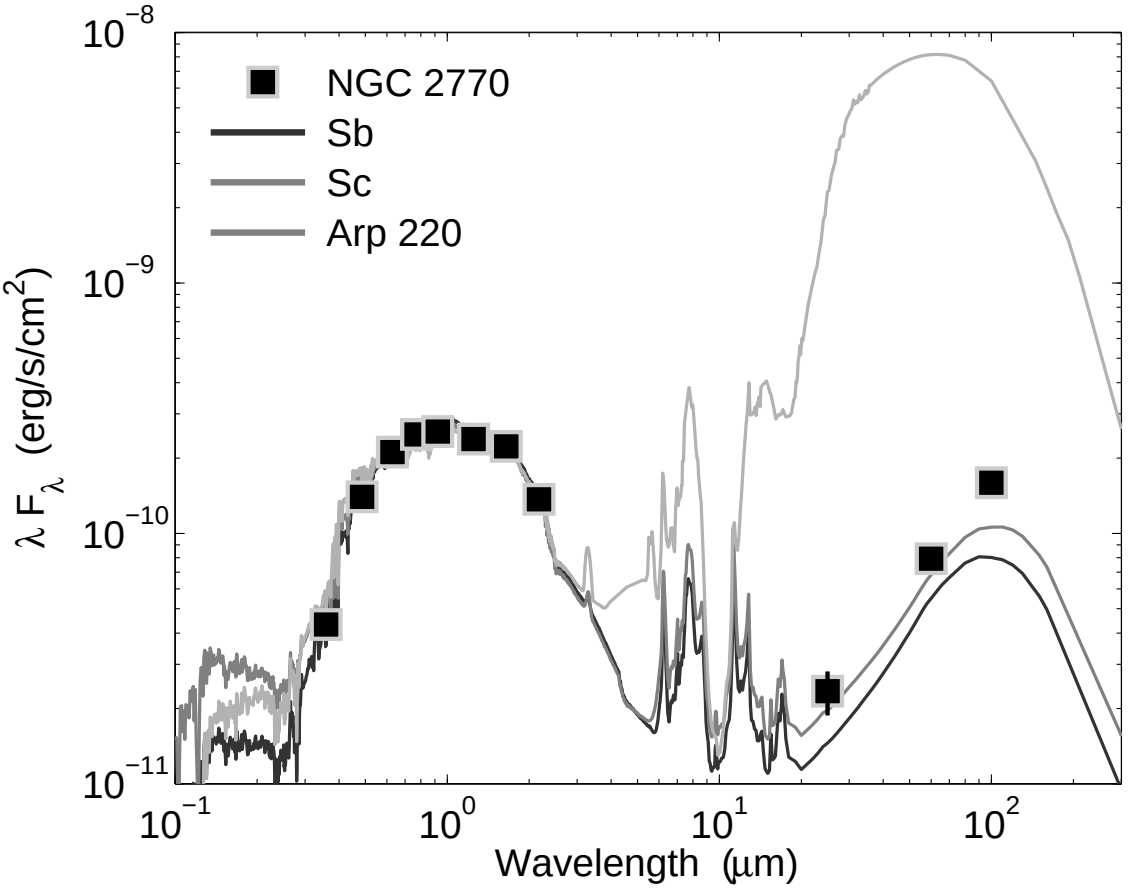

Figure 8. Optical to far-IR spectral energy distribution of NGC 2770. The data (black squares) are from the Sloan Digital Sky Survey (*ugriz* bands), the Two Micron All Sky Survey (*JHK* bands), and the Infrared Astronomical Satellite ($12 - 100$ μm). Also shown are Sb and Sc spiral galaxy models, as well as the SED of the galaxy Arp 220. The models are from the Spitzer Wide-area Infrared Extragalactic survey (SWIRE) template library. The data for NGC 2770 are in excellent agreement with the spiral galaxy models, but the weak FIR emission clearly rules out an extreme starburst origin (as for Arp 220).

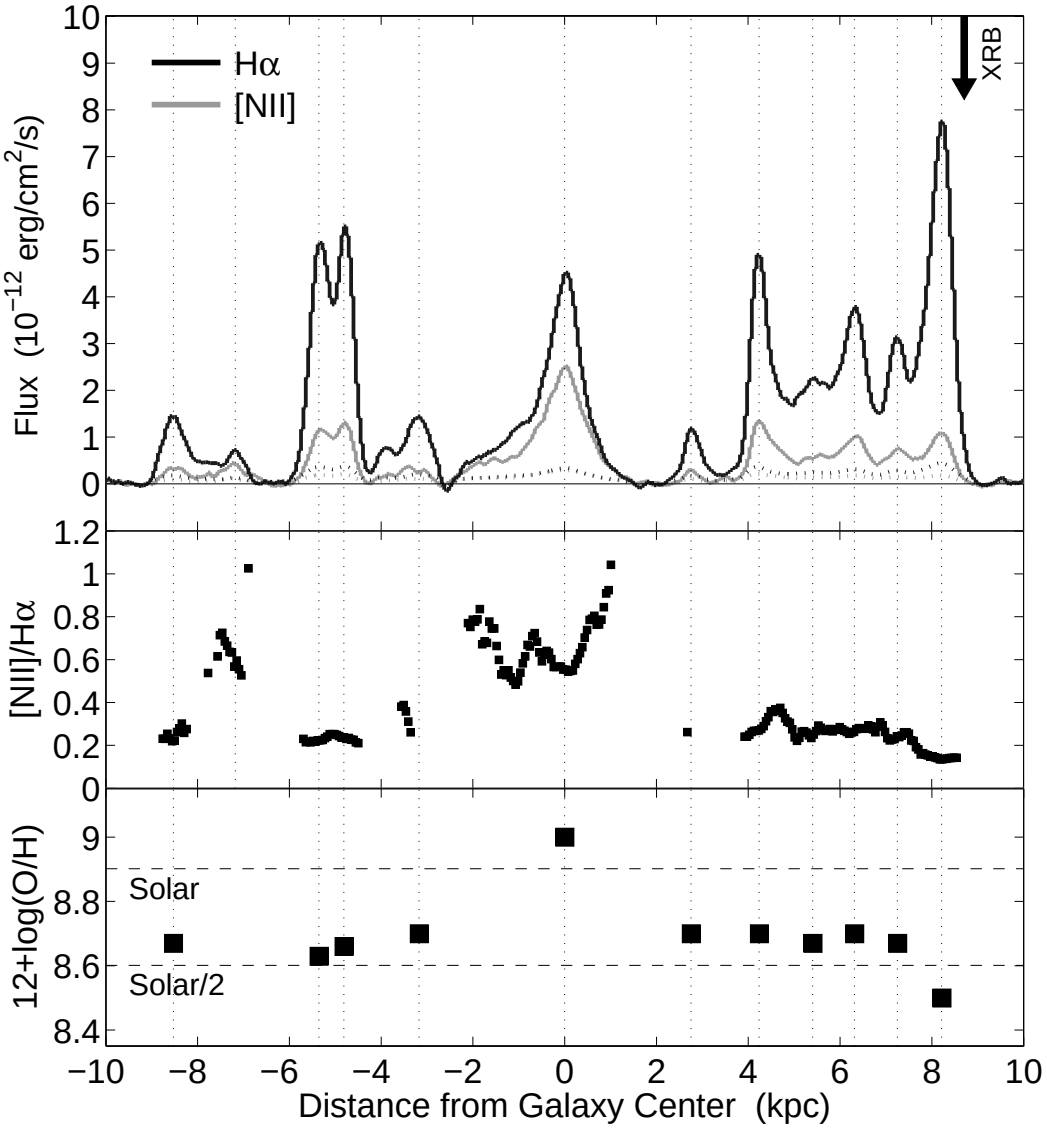

Figure 9. Metallicity of HII regions in NGC 2770 as a function of galactocentric radius. The top panel shows the profile along the slit of the Balmer Hα emission line (black line) and the [NII]λ6583 emission line (grey line), covering a range of $\pm$9 kpc from the center of NGC 2770. The underlying uniform emission from the galaxy has been removed in order to isolate the emission of the HII regions. The thick dotted lines designate the noise level for each emission line. The middle panel shows the ratio [NII]/Hα for regions of the slit that have a signal-to-noise, $S/N > 3$ in both lines. This ratio provides a measure of the metallicity. In the bottom panel we plot the metallicity $[12 + \log(\mathrm{O/H})]$ for each HII region using a wide range of emission lines and the formulation of.[58] The conversion between [NII]/Hα and metallicity depends on the ionization parameter, which we estimate using the ratio of oxygen lines, [OIII]λ5007/[OII]$\lambda\lambda$3726, 3729. We find $\log q = 7.5 \pm 0.2$. The resulting metallicities range from about 1.5 times the Solar metallicity near the center of the galaxy to about 0.5 times the Solar metallicity at its outskirts. Estimates of the metallicity in these HII regions from other line ratios (e.g., [NII]/[OII]) indicate a systematic uncertainty of about 0.2 dex in the values shown in the bottom panel.